ACS OMEGA

http://pubs.acs.org/journal/acsodf

Article

Data-Driven Optimization and Experimental Validation for the Lab-Scale Mono-Like Silicon Ingot Growth by Directional Solidification

Xin Liu,* Yifan Dang, Hiroyuki Tanaka, Yusuke Fukuda, Kentaro Kutsukake, Takuto Kojima, Toru Ujihara, and Noritaka Usami

Cite This: *ACS Omega* 2022, 7, 6665−6673

Read Online

ACCESS | Metrics & More | Article Recommendations

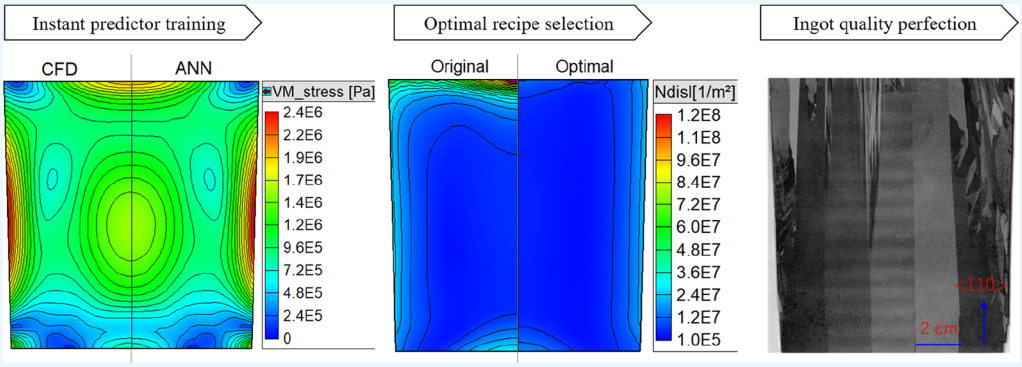

ABSTRACT: The casting mono-like silicon (Si) grown by directional solidification (DS) is promising for high-efficiency solar cells. However, high dislocation clusters around the top region are still the practical drawbacks, which limit its competitiveness to the monocrystalline Si. To optimize the DS-Si process, we applied the framework, which integrates the growing experiments, transient global simulations, artificial neuron network (ANN) training, and genetic algorithms (GAs). First, we grew the Si ingot by the original recipe and reproduced it with transient global modeling. Second, predictions of the Si ingot domain from different recipes were used to train the ANN, which acts as the instant predictor of ingot properties from specific recipes. Finally, the GA equipped with the predictor searched for the optimal recipe according to multi-objective combination, such as the lowest residual stress and dislocation density. We also implemented the optimal recipe in our mono-like DS-Si process for verification and comparison. According to the optimal recipe, we could reduce the dislocation density and smooth the growth rate during the Si ingot growing process. Comparisons of the growth interface and grain boundary evolutions showed the decrease of the interface concavity and the multi-crystallization in the top part of the ingot. The well-trained ANN combined with the GA could derive the optimal growth parameter combinations instantly and quantitatively for the multi-objective processes.

1. INTRODUCTION

The directional solidification (DS) process is widely used for several types of silicon (Si) ingot growth.[1] Based on the conventional multi-crystalline Si (mc-Si), the cast mono-like Si method was proposed for the cost-effective fabrication of Si solar cells.[2] Thus, the main body of the ingot, which has the monocrystalline structure, can realize the high-power conversion efficiency. Recently, the Seed Manipulation for Artificially Controlled Defect Technique (SMART)[3] has been expected to be a better choice for high-efficiency solar cell processing on cast mono-like Si by inhibiting the multi-crystallization along the crucible wall.[4] However, the bottom red zone because of the metal contamination and the high dislocation region at the top of the ingot are still the practical drawbacks, which limited its competitiveness to the monocrystalline Si grown by the Czochralski method.[5] Crystal structures and properties of the mono-like DS-Si ingots depend on the seed arrangement, growth interface evolution, generation and propagation of dislocations, thermal stress relaxation, impurity transport, etc. Especially, the high dislocation density gives negative influence on the conversion efficiency of solar cells by providing not only recombination sites for minority carriers but also shunt regions for majority carriers.[6] Therefore, it is crucial to control and optimize the thermal process of DS-Si for realizing the high percentage

Received: October 27, 2021
Accepted: February 7, 2022
Published: February 17, 2022

https://doi.org/10.1021/acsomega.1c06018
ACS Omega 2022, 7, 6665−6673

monocrystalline and low dislocation density in mono-like Si ingot.

The design of a DS-Si furnace and optimization of multiple process parameters require tremendous effort and professional knowledge owing to their nonlinear interactions. Extensive experimental[7−10] and numerical works[11−14] have been conducted on the parameter studies and the designs of recipe or geometry to realize the cast monocrystallization in the entire ingot. These qualitative analyses offer a deep understanding of the correlations among the input parameters and ultimate objectives of the DS-Si process. However, quantitative optimization and optimal design are still challenging tasks for this nonlinear dynamic process, which includes many coupled controlling elements to affect ingot quality properties.

Recently, data-driven modeling methods have shown great potential in modeling complex industrial processes.[15−21] Machine learning integrated with optimization algorithms has been successfully implemented for the geometrical design of the crystal growth systems[22] and the adaptive control of process parameters to speed up the optimization.[23] They applied optimization algorithms to get and parameterize the best combination of different controlling elements.[24,25] According to this integrated approach, the training data preparation is the prerequisite for the accurate machine learning model. However, massive growing experiments are expensive and time-consuming for the training data generation. Therefore, the reliable global simulation for the DS-Si process could be a trade-off option for the artificial neuron network (ANN) model training and the following genetic algorithm (GA) optimization. The key point is the reliability of the numerical model in this integrated optimization framework, including computational fluid dynamics (CFD), ANN, and GA. Therefore, experimental validations for the original and optimal recipe must be performed to guarantee the optimization performance. Besides validating heating profiles, many detailed validations for the ingot properties are essential for this integrated framework.[26]

Another advantage of the ANN application is the acceleration of CFD simulation to derive the GA database for process optimization. Tsunooka et al.[15] proposed the rapid flow pattern prediction by combining the CFD simulation and machine learning. Combined with their approach, the efficiency of GA optimization for the local or global, steady, or transient simulations can be improved. Some intermediate parameters, such as growth interface deflection, or the stress and dislocation of the monitored locations, were chosen as the objective functions. However, it is difficult to validate these intermediate parameters by the final ingot quality. Fast prediction and optimization for the quality properties and growing interface evolution of the entire ingot are preferable for the DS-Si optimization framework. In the final ingot from the mono-like DS-Si process, the dislocations decrease the conversion efficiency, whereas the residual stress can cause the crystals to fracture. It is desirable to connect the ingot quality properties and the input parameters by the rapid response database directly.

The present study focuses on optimizing the DS-Si process by the integrated framework, including transient global modeling, machine learning, optimization algorithm, and growing experiments. A lab-scale mono-like DS-Si furnace was taken as an application example. First, the validated 2D transient simulations with the real controlling parameter and recipe settings were performed to prepare the training data set for the machine learning model. Then, the ANN was well trained as the instant predictor, which could predict the Si ingot properties, such as the residual stress, dislocation density, and growth rate. Finally, the multi-objective GA was employed to search for the optimum recipes for the lowest stress and dislocation density with a stable growth rate. The ingots grown by the original recipe and the optimal recipe were compared in different measurement scales.

2. EXPERIMENTAL METHODS AND NUMERICAL FORMULATIONS

The optimization framework includes four parts: lab-scale growing experiment, transient global modeling, ANN training, and GA optimization. The lab-scale DS-Si furnace was the proof-of-concept (PoC) system for a growth of ∼100 mm square ingot. We built the 2D transient global model to predict the full process from melting to annealing the mono-like DS-Si process. The final results of the entire Si ingot domain from different recipes were used to train the ANN, which acts as an instant predictor from the growth recipe to the quality properties. Then, the GA equipped with the predictor could search for the optimal recipe according to the multi-objective combination. Finally, the validation of the optimal recipe was performed by our PoC system of DS-Si.

2.1. PoC Growing System of DS-Si. The schematic of the DS-Si furnace for the growing experiments and their transient global simulations is shown in Figure 1. Five mono-Si bricks of

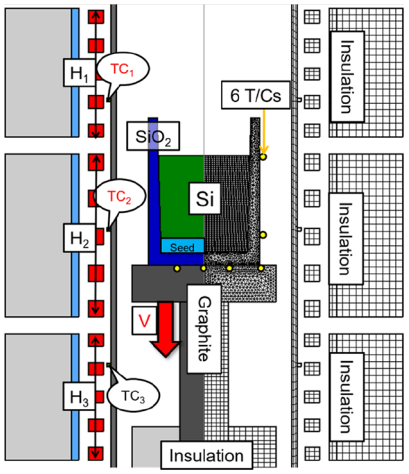

Figure 1. Schematic of the DS-Si furnace for the growing experiments and their transient global simulations.

100 × 20 × 50 (mm^3) were first placed as the seeds in a rectangular quartz crucible, which could grow the mono-like Si ingot of 112.5 × 112.5 × 130 (mm^3). Then, the poly-Si feedstock of 2200 g was loaded above the 50 mm mono-Si seed of ⟨110⟩ orientation. The solidification process is realized by lowering the crucible from the high-temperature zone to the low-temperature zone with an imposed speed, which was controlled by three three heating modules (H1: upper, H2: middle, and H3: lower), and the vertical moving of the crucible, respectively. Six thermocouples (T/Cs) were installed along the bottom and sidewall of the crucible to monitor the growing conditions. The original growing recipe includes three temperature profiles (TC_1, TC_2, and TC_3) and the crucible movement profile (V).[27] The growing stage was designed with the three constant temperatures at H1 by TC_1, H2 by TC_2, and

https://doi.org/10.1021/acsomega.1c06018
ACS Omega 2022, 7, 6665−6673

H3 by TC_3, and the fixed crucible downward speed of V = 0.5 mm/min in 400 min, as listed in Table 1.

Table 1. Control Parameter in the Original Recipe

parameter	value
designed duration Δt (min)	400
H1 temperature TC_1 (K)	1783
H2 temperature TC_2 (K)	1733
H3 temperature TC_3 (K)	1553
crucible downward speed V (mm/min)	0.5

2.2. Transient Global Modeling of DS-Si. The commercial crystal growth simulator, CGSim, was used for the 2D transient global modeling of DS-Si, which includes the entire thermal process from melting to annealing.[28] According to the principle of equivalent volume method and thermal resistance approximation, we simplify the square crucible to a cylindrical shape to save the computational cost. The furnace components are divided into a series of blocks and mesh by a structured/unstructured combined grid, as shown in Figure 1. Equations of mass, momentum, and energy were solved by the finite volume method. As mentioned in our previous works,[24,25] the major assumptions of the model are as follows: (1) the Si melt flow is incompressible, and the Boussinesq assumption is applied; (2) the geometry of the furnace is axisymmetric; and (3) all radiative surfaces are diffuse-gray. The three-level second-order implicit method is applied for the approximation of time derivatives. The temperature of the outer wall of the chamber and the time step are set as 300 K and 30 s, respectively.

Same with the growing experiment, three heating modules were realized by the PID (proportional−integral−derivative) controllers of TC_1, TC_2, and TC_3. To verify the heat transport model, the monitored temperatures along the crucible wall were compared with the experimental measurements. Figure 2a shows the temperature comparison at two of the monitored locations, which were set at the outer crucible sidewall by 40 and 130 mm above the crucible platform corresponding to the initial Si melt domain in the crucible. During the melting stage, the volume and conductivity of the loaded Si feedstock differs from the numerical model because of the porous packing structure.[29] Thus, the discrepancies between simulation and measurement are slightly higher than other stages. Since the presented work focused on the growing stage optimization, we could observe that the discrepancy is acceptable for the growing stage. Further, the temperature gradient from the preserved seed to the melt free surface was also fitted well by the transient global model. The growing interface evolution was also validated with the measurements, as shown in Figure 2b. We reproduced the growing interface evolution by the phosphorus doping contours, which are indicated by the resistivity measurement of the wafers. Even the preserved maximum seed height fitted well with the growing experiment, the convexity or concavity of interface was underestimated slightly due to the 2D axisymmetric simplification. Nevertheless, the accuracy of the 2D transient modeling is acceptable for this nonlinear and multi-physics system.

The build-in Haasen−Alexander−Sumino (HAS) model[30,31] was used to predict the stress and dislocation distributions in the growing Si ingot. The reliability of the HAS model has validated for the predictions of the stress and dislocation of the DS-Si ingot.[32,33] In this model, the total strain ε_{ij} is assumed to be subdivided into three components

$$\varepsilon_{ij} = \varepsilon_{ij}^{e} + \varepsilon_{ij}^{T} + \varepsilon_{ij}^{c} \tag{1}$$

that are the elastic ε_{ij}^{e}, thermal ε_{ij}^{T}, and creep ε_{ij}^{c}, respectively. The creep strain rate is related to the dislocation density. The creep strain rate and the multiplication rate of mobile dislocation density N_m are as follows

$$\dot{\varepsilon}_{ij}^{c} = \frac{1}{2} b k_0 (\tau_{eff})^{p} \exp\left(-\frac{Q}{kT}\right) N_m \frac{1}{\sqrt{J_2}} S_{ij} \tag{2}$$

$$\dot{N}_m = K k_0 (\tau_{eff})^{p+\lambda} \exp\left(-\frac{Q}{kT}\right) N_m \tag{3}$$

$$\tau_{eff} = \mathrm{Max}[0, \sqrt{J_2} - D\sqrt{N_m}] \tag{4}$$

$$J_2 = \frac{1}{2}\sum_{i,j} S_{ij}^2 \tag{5}$$

$$S_{ij} = \sigma_{ij} - \delta_{ij}\frac{1}{3}\sum_{k} \sigma_{kk} \tag{6}$$

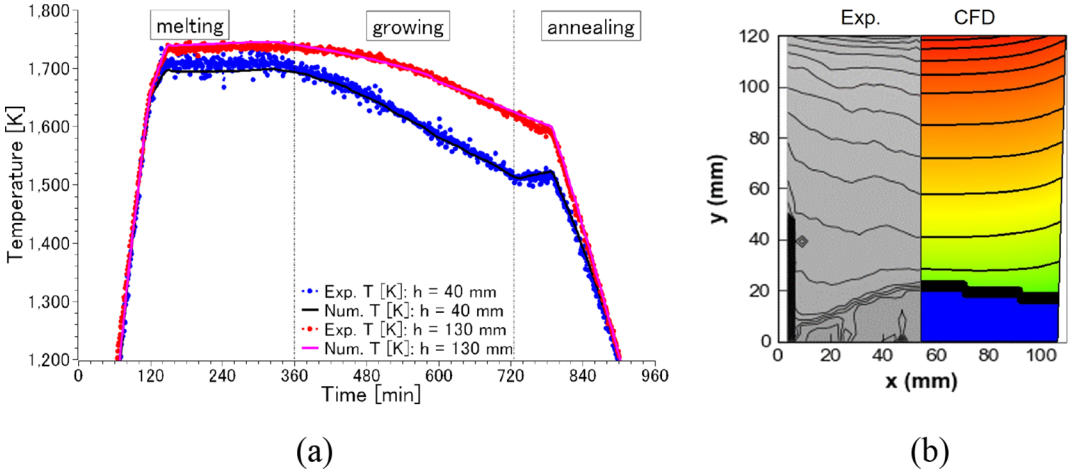

Figure 2. Growing experiment validations for the original recipe. (a) Comparison of monitored temperature profiles at the outer crucible sidewall (40 and 130 mm above the crucible platform) and (b) comparison of the growing interface evolutions in the growing stage.

https://doi.org/10.1021/acsomega.1c06018
ACS Omega 2022, 7, 6665−6673

where b is the magnitude of the Burgers vector, τ_{eff} is the effective stress, Q represents the Peierls potential, k is Boltzmann's constant, T is the absolute temperature in the Si ingot, S_{ij} stands for deviatoric stress tensor components, J_2 represents the second invariant of the deviatoric stress, and D stands for the strain hardening factor. k_0, K, p, and λ are material constants, and σ_{ij} denotes the stress tensor components. The crystal anisotropy was neglected, and the boundary conditions of stress along the crucible wall are set by the free boundaries due to the coating. The von Mises stress σ_{von} is used to represent the residual stress components and defined as

$$\sigma_{von} = \left(\frac{3}{2} S_{ij} S_{ij}\right)^{1/2} \tag{7}$$

Here, we also considered the stress during the melting stage.

2.3. GA Coupled with 2D Predictor from ANN. Heating profiles of the three heating modules and the crucible downward speed are the primary input parameters in the recipe for this DS-Si process. We built the ANN prediction model to explore the mapping relationship between the controlling parameters and ingot quality properties. A typical ANN comprises three layers (input, hidden, and output) of neurons and synapses, where the synapses' function is to transmit information. Each neuron receives inputs and processes them before giving outputs. The most common output operation for the j-th neurons in hidden or output layers is shown as

$$O_j = A\left(\sum_{i=1}^{n} \omega_{j,i} \cdot x_i + b_i\right) \tag{8}$$

where $\omega_{j,i}$ denotes the weight of connection from the i-th neuron of the preceding layer to the current neuron. b_i and A are bias and activation functions, respectively.

Since the maximum temperature of H3 is lower than the melting point of Si, it could not affect the growing stage on which we were focusing. The upper heater (H1), middle heater (H2), and the crucible downward speed were chosen as the inputs of the ANN model, as well as the mesh coordinates (r, z) of the ingot domain (51 × 51 points). Temperature adjustments of H1 and H2 during the growing stage were defined by ΔTC_1 and ΔTC_2, while the adjustment of the crucible downward speed is defined by dV. The outputs were the residual stress, the dislocation density, and the solidification time for every grid (r, z) of the final Si ingot. With the validated transient global model, 150 combinations of three inputs, including the crucible movement and temperature profile of two heaters, were simulated to prepare the training data for the ANN. The total data are 150 sets with (51 × 51) points, and they are divided randomly by 120 cases and 30 cases for training and test, respectively. It means (150 × 51 × 51) data sets for ANN training because of the coordinate (r, z) mapping. The ANN was well trained as the predictor, which could instantly predict the Si ingot properties, such as the solidification time, the dislocation density, and the stress level for the entire domain of the final ingot. We employed NSGA-II[34] to search for the optimal recipe for the lowest residual stress and dislocation density and the shortest solidification time. Figure 3 shows the operational flow of the GA coupled with a predictor of the ANN.

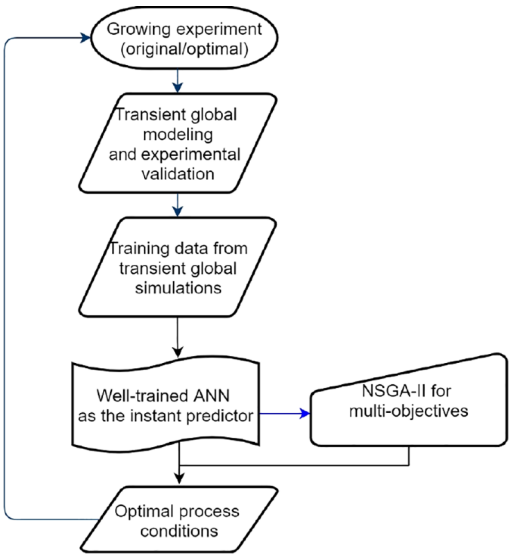

Figure 3. Operational flow of the GA coupled with a predictor from the ANN.

3. RESULTS AND DISCUSSION

3.1. Preliminary Analysis of the Original Process. Generally, the DS-Si process includes three stages: melting, growing, and annealing. Every stage of the recipe is designed to realize different targets. For the melting stage, a certain height of mono-Si seed must be kept for the mono-like DS-Si process. During the growing stage, the growth interface evolution and growth rate have to be well controlled to obtain the high percentage of monocrystalline structure. Finally, the annealing stage should prevent dislocation generation because of the thermal stress relaxation. According to the growing experiments with the original recipe, there were three disadvantages in the growing process. First, the growing stage was always out of the designed duration of about 30 min, when the heating profile has started the designed annealing stage. Second, the growing interface kept high concavity (Figure 2b) in most of the growing time, which is harmful to the uniformities of impurity and dopants in the final ingot. Third, multicrystallization occurred around the crucible wall and top surface, which destroyed the designed vertical grain growth in the upper part of the ingot. These disadvantages resulted in that the final ingots were easy to lose the monocrystalline structure in the later growth stage. The high concavity of the growing interface and inhomogeneous growth rates in horizontal and vertical directions are supposed to be the drawbacks of the original recipe. Therefore, we tried to optimize the casting process by adjusting the control parameters in the process recipe with a 300 min prolonged growing stage.

3.2. ANN Training Results from the CFD Data. For preparing the training data by the transient simulations, we set the ranges of the inputs, including ΔTC_1, ΔTC_2, dV, r, and z, as listed in Table 2. From the 150 sets of training data calculated by CFD simulations, we trained the ANN model to predict the quality properties in the ingot domain at position (r, z) from different process recipes. Table 3 lists the root-mean-square errors (RMSEs) of cross-validation for different hidden layers and neurons per layer. Our ANN was constructed with 5 hidden layers and 128 neurons in each layer, which achieved the lowest RMSE, while much more

https://doi.org/10.1021/acsomega.1c06018
ACS Omega 2022, 7, 6665−6673

Table 2. Training Data Ranges for Machine Learning

parameter	range	samples
H1 temperature change ΔTC_1 (K)	−30 to +30	5
H1 temperature change ΔTC_2 (K)	−30 to +30	5
crucible speed change dV (mm/min)	−0.5 to 0	6
radius (mm) r	0−57	51
height (mm) z	0−130	51

Table 3. RMSEs of Cross-Validation for the Different ANN Structures

RMSE	64 neurons	128 neurons
three layers	0.0059	0.0053
five layers	0.0055	0.0048
seven layers	0.0057	0.0050

hidden layer and neurons led to the unacceptable training efficiency. Figure 4 shows the performance of machine learning models on residual stress, dislocation density, and solidification time for a test case. The machine learning prediction results matched almost perfectly with the CFD simulation results for the three outputs. It indicated that the well-trained ANN model obtained the mapping relationship among process parameters and ingot quality properties. The well-trained ANN model could significantly speed up the predictions by more than 27 thousand times, while the entire process CFD simulation takes more than 6 h for a single case. Therefore, our prediction model could act as the instant predictor and data generator for the following NSGA-II optimization.

It is worth overviewing the effect of input parameters on the output parameters using linear analysis such as correlation analysis, although the ANN model is nonlinear. Figure 5 shows the correlation coefficients between inputs and outputs. The maximum residual stress and dislocation density showed negative correlations with the three inputs, as well as the mean dislocation density. In comparison, the maximum solidification time showed a positive correlation with the three inputs. Meanwhile, the crucible downward speed is related to all the four outputs by the high-correlation coefficients, which implies that the change of this crucible movement could be the most effective way for the process optimization. The solidification time and other outputs have the opposite correlation coefficients with the inputs, which

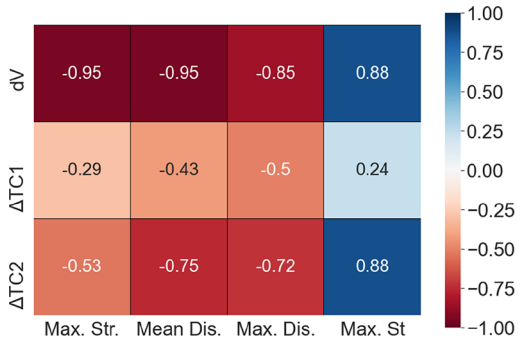

Figure 5. Correlation coefficients between process controlling parameters and ingot properties.

implies the trade-offs between fast growing and low dislocation density and residual stress.

3.3. NSGA-II Optimization. With the instant predictor, we introduced the GA to select the optimum parameter settings. We implemented NSGA-II with multi-objective functions for the lowest values. They are the maxima of residual stress, the dislocation density, and the solidification time, as well as the mean dislocation density. NSGA-II generated 160 random individuals in the unchanged parameter ranges and then recommended the optimum parameter settings based on different objective functions after 400 generations of evolution. The calculation compared (160 × 160 × 160) sets of inputs for the four objective combinations in less than 2 h. In addition, the algorithm proposed 160 recipes according to different objective combinations.

One advantage of NSGA-II is that we could select the optimal parameter settings for the major target from the Pareto fronts. Furthermore, the optimal growing condition could be derived quantitatively from the well-trained ANN, while the conventional parametric study could only show the qualitative tendency. Figure 6a shows the plots of the Pareto fronts for the maxima of residual stress and dislocation as the functions of solidification duration. For our PoC system, we prefer the lowest dislocation (mean and maximum) as the major target for the growing experiment design. Thus, we selected the lowest dislocation density with relatively shorter solidification duration and lower residual stress as the optimal recipe, as marked in Figure 6a. The selected optimum parameter setting is ΔTC_1 = −13.4 K, ΔTC_2 = 28.5 K, and dV = −0.5 mm/min.

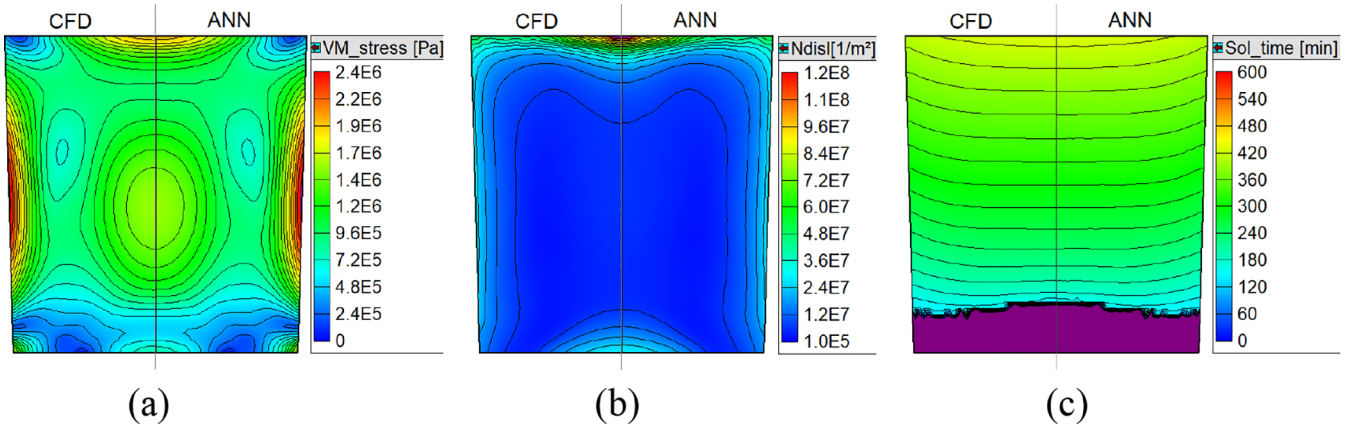

Figure 4. CFD results (left) and ANN predictions (right) for (a) residual stress, (b) dislocation density, and (c) solidification time or interface shape.

https://doi.org/10.1021/acsomega.1c06018
ACS Omega 2022, 7, 6665−6673

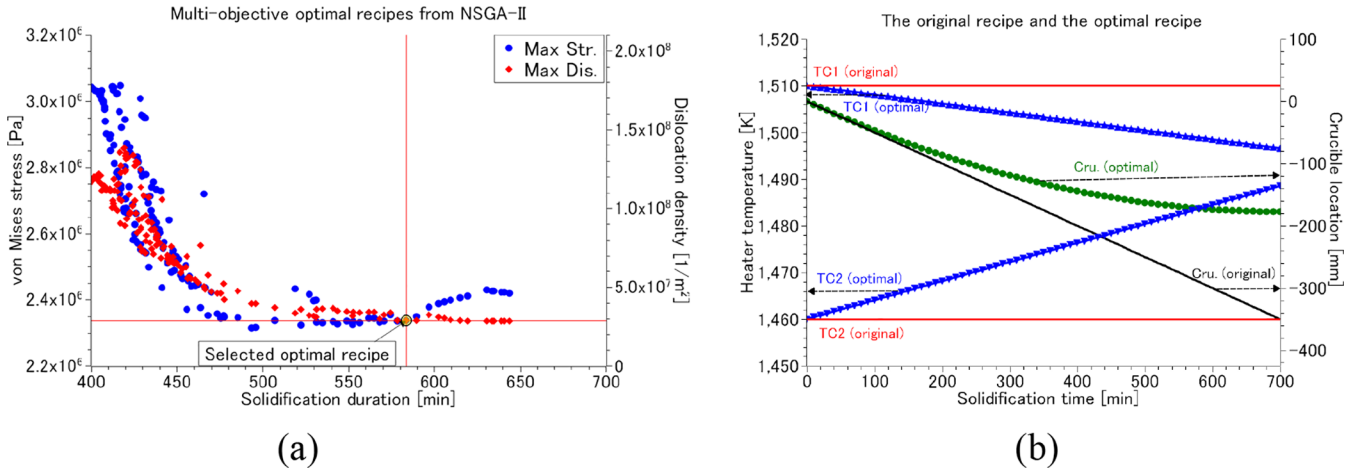

Figure 6. NSGA-II optimization results. (a) Multi-objective optimal recipes from NSGA-II and (b) selected optimal recipe for the growing stage.

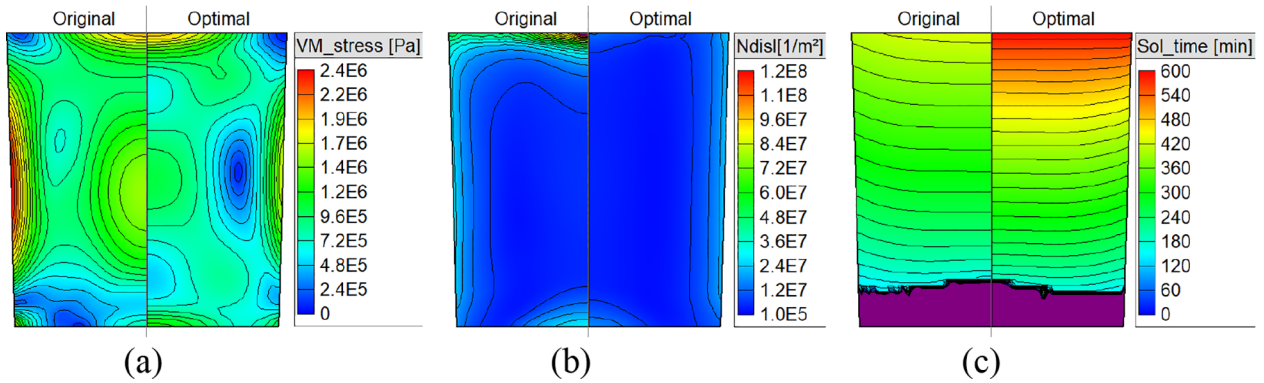

Figure 7. Comparison of quality properties including (a) residual stress, (b) dislocation density, and (c) growing interface evolution and solidification time in a final Si ingot cross section between the original recipe (left) and the optimal recipe (right).

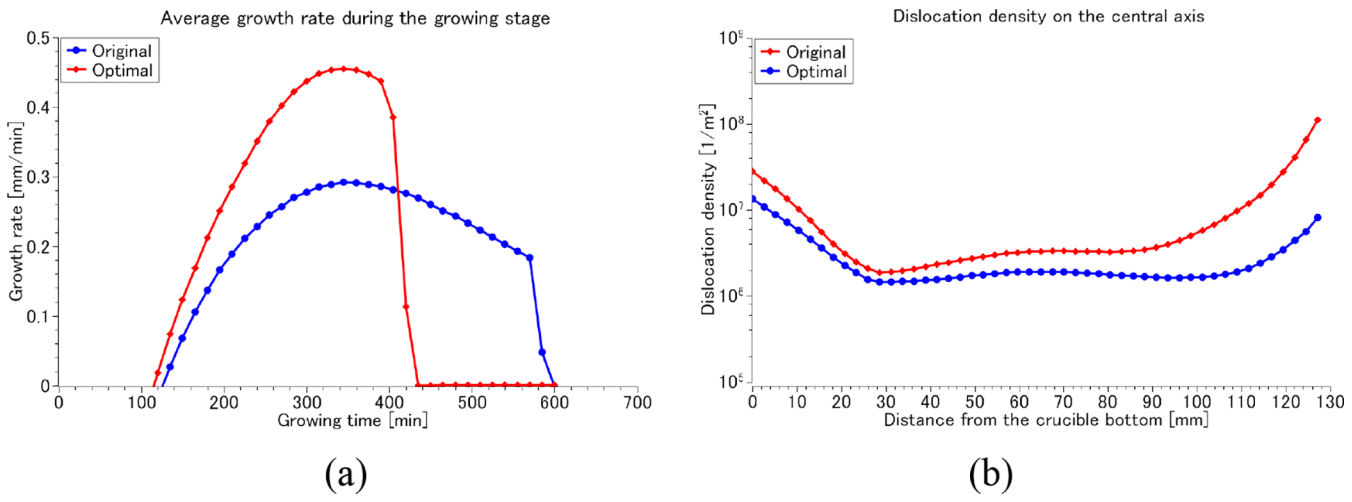

Figure 8. Optimization results of growth rate and dislocation density in the Si ingot. (a) Stabilized growth rate by slowing down crucible downward and (b) dislocation reduction along the central axis of the ingot.

Figure 6b shows the details of the selected optimal recipe for the 700 min growing stage. Compared to the original recipe, the optimal recipe indicated the slowing down crucible downward, the temperature decrease of the TC1, and the temperature increase of TC2.

We could feed the optimal recipes into the well-trained ANN to get the detailed ingot properties instantly. We could also conduct the transient global simulation to validate the optimal recipe. Figure 7 compares quality properties in the final Si ingot cross section between the original recipe (left) and the optimal recipe (right). The residual stress distributions showed similar patterns for the original and optimal cases, while the maximum stress along the crucible wall and top surface decreased about 20%, as shown in Figure 7a. Since we focused on the dislocation reduction, the optimal recipe got a maximum dislocation density of 2.2×10^7 1/m^2. It achieved a

https://doi.org/10.1021/acsomega.1c06018
ACS Omega 2022, 7, 6665−6673

low-level dislocation in the top part of the ingot with a 84% reduction of maximum dislocation, as shown in Figure 7b. In the monocrystalline area, the dislocation density is also decreased from 5.5 × 10^6 1/m^2 in the original ingot to 3.8 × 10^6 1/m^2 in the optimized ingot. The interface evolutions of the optimal recipe in the right section of Figure 7c implied an interface shape transition from concave to flat but 164 min longer solidification time.

As shown in Figure 8a, the original recipe showed faster growth, while the optimal recipe decreased the growth rate. The high growth rate of the original recipe resulted in high dislocation in the upper half of the ingot (Figure 8b). The optimal recipe smoothed the growth rate by slowing down the crucible and decrease of temperature gradient in the upper half of the ingot. The smoothed growth rate relaxed the stress release at the end of the growing and transition stage, which resulted in the remarkable dislocation reduction, as shown in Figure 8b. Even the crucible was almost stopped finally, the lowest growth rate was 0.2 mm/min due to the cooling effect of gas flow.

3.4. Optimal Recipe Validation by Growing Experiment. The optimal recipes recommended by NSGA-II were implemented in our mono-like DS-Si process for verification and comparison. Except for the optimized controlling parameters, other growing conditions were kept the same as the original recipe. Wafers for evaluation were cut out of the ingots with a thickness of 1 mm. The slice was cut from the center of the five parallel seeds in the plane perpendicular to the crucible bottom and the long edge of the seeds. Figure 9

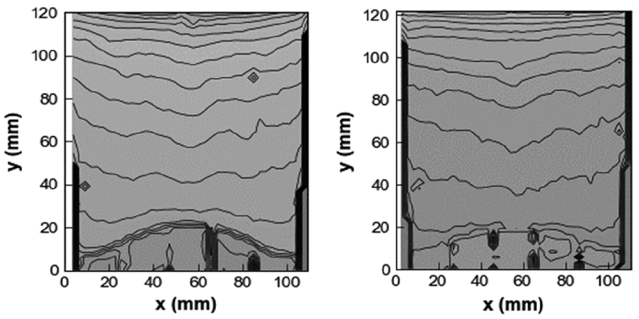

Figure 9. Growing interface evolution comparison between the original and optimal recipe. Reproduced interface shapes for (a) original recipe and (b) optimal recipe by resistivity contours in final ingots.

shows the growing interface comparison between the original and optimal recipe. With a fixed crucible downward speed of 0.5 mm/min, the initial growing interface of the original case started with a high convexity shape. The preserved seed in the center is much thicker than the periphery area of the crucible wall (Figure 9a). This is harmful to accurate controlling of the seed preservation height and seed arrangement cost. As the casting process proceeded, the growing interface experienced convex to concave transition, which showed a high deviation of growth rate from center to periphery. The concave interface that lasted until the end of the casting stage was also not preferable for the high-quality ingot growing. The optimal recipe recommended slowing down the crucible speed from 0.5 mm/min to 0. Since the solidification started about 90 min later than the crucible downward-moving started, the initial growing interface on the higher crucible position was much flatter than the original case, as shown in Figure 9b. This is favorable for accurate controlling of the seed preservation height and the vertical grain growth. Because of the aspect ratio of the small crucible, the growing interface also switched to a concave shape with the casting process proceeded. However, the growing interface became flat at the end of solidification, which differed from the original case. The almost stagnant crucible at the end of solidification in the optimal case resulted in a low growth rate, which might be dominated by the gas flow cooling. This smoothed growth could reduce the multi-crystallization in the top part of the ingot.

Figure 10 shows the grain growth comparison between the original and optimal recipe. We took optical images for the

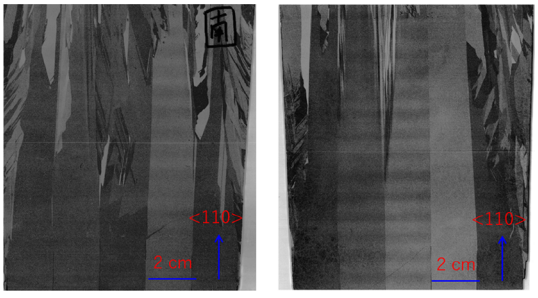

Figure 10. Grain growth comparison between the original and optimal recipe. Optical image of the original recipe (a) and the optimal recipe (b).

wafers, which sliced from the center of the ingots. The original case (Figure 10a) showed the expansion of the multi-crystallization zone from the crucible side wall to the top. The optimal case (Figure 10b) showed the decrease of the multi-crystallization in the top part of the ingot. The comparison verified the effectiveness of the optimal recipe for restraining multi-crystallization by the smoothed growth rate and the flatter growing interface. It is noted that the slower growth rate may decrease the yield in the practical industrial process. Thus, further optimization has to be conducted on the geometrical design of DS-Si growth by the optimization framework.

4. CONCLUSIONS

We proposed a general workflow, including CFD, machine learning, genetic optimization, and crystal growing experiment. In this framework, an instant predictor has been trained for the final crystal quality prediction. Optimal recipes for dislocation reduction were recommended by NSGA-II and validated by CFD. We also implemented the optimal recipe in our mono-like DS-Si process for verification and comparison. According to the optimal recipe, the low dislocation density and smoothed growth rate were achieved in the Si ingot growing process. Comparisons of the growth interface and grain boundary evolutions implied the decreases of the interface concavity and the multi-crystallization in the top part of the ingot. Further optimization is also possible and essential for the geometry design to realize the little convex growing interfaces during the entire growing process. The presented workflow is also applicable for the instant prediction and quantitative optimization of other multi-parameter processes.

https://doi.org/10.1021/acsomega.1c06018
ACS Omega 2022, 7, 6665−6673

AUTHOR INFORMATION

Corresponding Author

Xin Liu − *Graduate School of Engineering, Nagoya University, Nagoya 464-8603, Japan;* orcid.org/0000-0003-0832-327X; Email: liu.xin@material.nagoya-u.ac.jp

Authors

Yifan Dang − *Graduate School of Engineering, Nagoya University, Nagoya 464-8603, Japan;* orcid.org/0000-0003-4948-1178

Hiroyuki Tanaka − *Graduate School of Engineering, Nagoya University, Nagoya 464-8603, Japan*

Yusuke Fukuda − *Graduate School of Engineering, Nagoya University, Nagoya 464-8603, Japan*

Kentaro Kutsukake − *Center for Advanced Intelligence Project, RIKEN, Tokyo 103-0027, Japan*

Takuto Kojima − *Graduate School of Informatics, Nagoya University, Nagoya 464-8603, Japan*

Toru Ujihara − *Graduate School of Engineering, Nagoya University, Nagoya 464-8603, Japan; Institute of Materials and Systems for Sustainability, Nagoya University, Nagoya 464-8601, Japan*

Noritaka Usami − *Graduate School of Engineering, Nagoya University, Nagoya 464-8603, Japan*

Complete contact information is available at: https://pubs.acs.org/10.1021/acsomega.1c06018

Notes

The authors declare no competing financial interest.

ACKNOWLEDGMENTS

This work was partially supported by JST/CREST, grant no. JPMJCR17J1 (2017−2023).

REFERENCES

(1) Nakajima, K. Basic growth and crystallographic quality of Si crystals for solar cells. In *Crystal Growth of Si Ingots for Solar Cells Using Cast Furnaces*; Nakajima, K., Ed.; Elsevier, 2020; Chapter 1, pp 1−61.

(2) Wang, P.; Cui, C.; Yang, D.; Yu, X. Seed-Assisted Growth of Cast-Mono Silicon for Photovoltaic Application: Challenges and Strategies. *Sol. RRL* **2020**, *4*, 1900486.

(3) Takahashi, I.; Joonwichien, S.; Iwata, T.; Usami, N. Seed manipulation for artificially controlled defect technique in new growth method for quasi-monocrystalline Si ingot based on casting. *Appl. Phys. Express* **2015**, *8*, 105501.

(4) Schubert, M. C.; Schindler, F.; Benick, J.; Riepe, S.; Krenckel, P.; Richter, A.; Müller, R.; Hammann, B.; Nold, S. The potential of cast silicon. *Sol. Energy Mater. Sol. Cells* **2021**, *219*, 110789.

(5) Song, L.; Yu, X. Defect engineering in cast mono-like silicon: A review. *Prog. Photovoltaics Res. Appl.* **2021**, *29*, 294−314.

(6) Takahashi, I.; Usami, N.; Kutsukake, K.; Stokkan, G.; Morishita, K.; Nakajima, K. Generation mechanism of dislocations during directional solidification of multicrystalline silicon using artificially designed seed. *J. Cryst. Growth* **2010**, *312*, 897−901.

(7) Kutsukake, K.; Usami, N.; Ohno, Y.; Tokumoto, Y.; Yonenaga, I. Mono-Like Silicon Growth Using Functional Grain Boundaries to Limit Area of Multicrystalline Grains. *IEEE J. Photovolt.* **2014**, *4*, 84−87.

(8) Lan, C. Y.; Wu, Y. C.; Lan, A.; Yang, C. F.; Hsu, C.; Lu, C. M.; Yang, A.; Lan, C. W. Control of ingot quality and solar cell appearance of cast mono-like silicon by using seed partitions. *J. Cryst. Growth* **2017**, *475*, 136−143.

(9) Trempa, M.; Reimann, C.; Friedrich, J.; Müller, G.; Krause, A.; Sylla, L.; Richter, T. Defect formation induced by seed-joints during directional solidification of quasi-mono-crystalline silicon ingots. *J. Cryst. Growth* **2014**, *405*, 131−141.

(10) Ekstrøm, K. E.; Stokkan, G.; Søndenå, R.; Dalaker, H.; Lehmann, T.; Arnberg, L.; Di Sabatino, M. Structure and dislocation development in mono-like silicon. *Phys. Status Solidi A* **2015**, *212*, 2278−2288.

(11) Ma, W.; Zhong, G.; Sun, L.; Yu, Q.; Huang, X.; Liu, L. Influence of an insulation partition on a seeded directional solidification process for quasi-single crystalline silicon ingot for high-efficiency solar cells. *Sol. Energy Mater. Sol. Cells* **2012**, *100*, 231−238.

(12) Qi, X.; Zhao, W.; Liu, L.; Yang, Y.; Zhong, G.; Huang, X. Optimization via simulation of a seeded directional solidification process for quasi-single crystalline silicon ingots by insulation partition design. *J. Cryst. Growth* **2014**, *398*, 5−12.

(13) Su, W.; Li, J.; Yang, W.; Han, X.; Guan, Z.; Zhang, Z. Numerical Investigation of Bottom Grille for Improving Large-Size Silicon Quality in Directional Solidification Process. *Silicon* **2022**, *14*, 211.

(14) Yu, Q.; Liu, L.; Ma, W.; Zhong, G.; Huang, X. Local design of the hot-zone in an industrial seeded directional solidification furnace for quasi-single crystalline silicon ingots. *J. Cryst. Growth* **2012**, *358*, 5−11.

(15) Tsunooka, Y.; Kokubo, N.; Hatasa, G.; Harada, S.; Tagawa, M.; Ujihara, T. High-speed prediction of computational fluid dynamics simulation in crystal growth. *CrystEngComm* **2018**, *20*, 6546−6550.

(16) Fühner, T.; Jung, T. Use of genetic algorithms for the development and optimization of crystal growth processes. *J. Cryst. Growth* **2004**, *266*, 229−238.

(17) Su, J.; Chen, X.; Li, Y.; Pons, M.; Blanquet, E. A niching genetic algorithm applied to optimize a SiC-bulk crystal growth system. *J. Cryst. Growth* **2017**, *468*, 914−918.

(18) Asadian, M.; Seyedein, S. H.; Aboutalebi, M. R.; Maroosi, A. Optimization of the parameters affecting the shape and position of crystal−melt interface in YAG single crystal growth. *J. Cryst. Growth* **2009**, *311*, 342−348.

(19) Dropka, N.; Holena, M. Optimization of magnetically driven directional solidification of silicon using artificial neural networks and Gaussian process models. *J. Cryst. Growth* **2017**, *471*, 53−61.

(20) Ren, J.-C.; Liu, D.; Wan, Y. Modeling and application of Czochralski silicon single crystal growth process using hybrid model of data-driven and mechanism-based methodologies. *J. Process Control* **2021**, *104*, 74−85.

(21) Kutsukake, K.; Nagai, Y.; Horikawa, T.; Banba, H. Real-time prediction of interstitial oxygen concentration in Czochralski silicon using machine learning. *Appl. Phys. Express* **2020**, *13*, 125502.

(22) Yu, W.; Zhu, C.; Tsunooka, Y.; Huang, W.; Dang, Y.; Kutsukake, K.; Harada, S.; Tagawa, M.; Ujihara, T. Geometrical design of a crystal growth system guided by a machine learning algorithm. *CrystEngComm* **2021**, *23*, 2695−2702.

(23) Dang, Y.; Zhu, C.; Ikumi, M.; Takaishi, M.; Yu, W.; Huang, W.; Liu, X.; Kutsukake, K.; Harada, S.; Tagawa, M.; Ujihara, T. Adaptive process control for crystal growth using machine learning for high-speed prediction: application to SiC solution growth. *CrystEngComm* **2021**, *23*, 1982−1990.

(24) Dang, Y.; Liu, L.; Li, Z. Optimization of the controlling recipe in quasi-single crystalline silicon growth using artificial neural network and genetic algorithm. *J. Cryst. Growth* **2019**, *522*, 195−203.

(25) Qi, X.; Ma, W.; Dang, Y.; Su, W.; Liu, L. Optimization of the melt/crystal interface shape and oxygen concentration during the Czochralski silicon crystal growth process using an artificial neural network and a genetic algorithm. *J. Cryst. Growth* **2020**, *548*, 125828.

(26) Dropka, N.; Holena, M. Application of Artificial Neural Networks in Crystal Growth of Electronic and Opto-Electronic Materials. *Crystals* **2020**, *10*, 663.

(27) Boucetta, A.; Kutsukake, K.; Kojima, T.; Kudo, H.; Matsumoto, T.; Usami, N. Application of artificial neural network to optimize sensor positions for accurate monitoring: an example with

thermocouples in a crystal growth furnace. *Appl. Phys. Express* **2019**, *12*, 125503.
(28) STR, US. *CGSim Theory Manual v. 20*; STR IP Holding, LLC: Richmond, VA, USA, 2019.
(29) Liu, X.; Nakano, S.; Kakimoto, K. Effect of the packing structure of silicon chunks on the melting process and carbon reduction in Czochralski silicon crystal growth. *J. Cryst. Growth* **2017**, *468*, 595−600.
(30) Alexander, H.; Haasen, P. Dislocations and Plastic Flow in the Diamond Structure. *Solid State Phys.* **1969**, *22*, 27−158 Seitz, F.; Turnbull, D.; Ehrenreich, H., Eds. Academic Press.
(31) Suezawa, M.; Sumino, K.; Yonenaga, I. Dislocation dynamics in the plastic deformation of silicon crystals. II. Theoretical analysis of experimental results. *Phys. Status Solidi A* **1979**, *51*, 217−226.
(32) Smirnova, O. V.; Mamedov, V. M.; Kalaev, V. V. Numerical Modeling of Stress and Dislocations in Si Ingots Grown by Seed-Directional Solidification and Comparison to Experimental Data. *Cryst. Growth Des.* **2014**, *14*, 5532−5536.
(33) Nakano, S.; Gao, B.; Jiptner, K.; Harada, H.; Miyamura, Y.; Sekiguchi, T.; Fukuzawa, M.; Kakimoto, K. Numerical analysis of the relation between dislocation density and residual strain in silicon ingots used in solar cells. *J. Cryst. Growth* **2017**, *474*, 130−134.
(34) Deb, K.; Pratap, A.; Agarwal, S.; Meyarivan, T. A fast and elitist multiobjective genetic algorithm: NSGA-II. *IEEE Trans. Evol. Comput.* **2002**, *6*, 182−197.

https://doi.org/10.1021/acsomega.1c06018
ACS Omega 2022, 7, 6665−6673